Journal of Materials Chemistry A

COMMUNICATION

View Article Online
View Journal | View Issue

Published on 02 February 2016. Downloaded by University of Tennessee at Knoxville on 02/06/2016 19:25:03.

Cite this: J. Mater. Chem. A, 2016, 4, 3238

Received 13th December 2015
Accepted 29th January 2016

DOI: 10.1039/c5ta10185a

www.rsc.org/MaterialsA

Synergistic carbon nanotube aerogel – Pt nanocomposites toward enhanced energy conversion in dye-sensitized solar cells

Haijun Chen,†[a] Tao Liu,†[a] Jing Ren,[a] Hongcai He,[a] Yonghai Cao,[b] Ning Wang*[a] and Zhanhu Guo*[b]

With the lab-made carbon nanotube aerogel (CNA) serving as the counter electrode (CE), dye-sensitized solar cells (DSSCs) operated under solar simulator illumination (100 mW cm^{-2}, AM 1.5 G) demonstrated an overall power conversion efficiency (η) of 8.35%, higher than the η of 5.95 and 7.39% of DSSCs with a multi-walled carbon nanotube (MWCNT) CE and conventional Pt CE, respectively. With only 3.75 wt% Pt nanoparticles to form an aerogel carbon nanotube composite (CNA-3.75 wt% Pt) CE, the corresponding η was further increased to 9.04%. The enhanced performance by introducing Pt nanoparticles is mainly attributed to the improved electrocatalytic activity, reduced charge-transfer resistance (R_{ct}) at the CE/electrolyte interface, and increased diffusion for the redox couple in the electrolyte. This work provides substantial support for developing low-cost Pt-loaded nanocomposite CEs to further enhance the DSSC performance.

1. Introduction

Renewable solar energy, with capabilities not only to solve energy crisis but also to protect environments, has attracted growing interest as an alternative to conventional fossil fuels. Since the innovative construction proposed by O'Regan and Grätzel in 1991,[1] dye-sensitized solar cells (DSSCs) have received significant attention as one of the most promising candidates for photovoltaic systems, due to their low manufacturing cost, facile fabrication process, eco-friendliness, and acceptable energy conversion efficiency (η).[2–5] A typical DSSC has a sandwich structure composed of a sensitizer dye adsorbed nanocrystalline TiO_2 photoanode covered on a fluorine-doped tin oxide (FTO) conductive glass substrate, a liquid electrolyte containing the iodide/triiodide (I^-/I_3^-) redox couple, and a catalytic counter electrode (CE).[3,4] All these components have been recognized to play significant roles in determining the performance of DSSC devices. Continuous efforts have been devoted to optimizing the DSSC components to further boost the η and stability of devices.[6–9] As one of the indispensable parts of DSSCs, the CE plays a pivotal role as a platform for collecting electrons from the external circuit back to the electrolyte and electrocatalytic reduction of I_3^- in the electrolyte.[10] A highly efficient CE can reduce inner energy losses in DSSCs and thus improve the device performance. So far, Pt has been widely used and recognized as a superior CE material for DSSCs due to its good electrical conductivity, long-term stability and excellent catalytic activity. However, the high price and limited availability of Pt metal have seriously impeded its practical deployment.[11–13] To solve this problem, the use of non-Pt CE materials with low-cost and high efficiency electrocatalytic activity for reducing I_3^- has been recognized as a promising approach, including various carbon materials,[2,14–18] metal sulfides,[10,19–23] metal nitrides,[24–26] metal carbides,[27] metal oxides,[11,28,29] alloys,[30,31] and conductive polymers.[32] However, few alternative electrodes have been reported with performances comparable to that of the conventional Pt CE in low-cost DSSC systems. Another way focusing on reducing the required amount of Pt by developing Pt-loaded nanocomposite catalysts[31,33,34] has been viewed as an attractive strategy due to the synergistic effect of different components of the composite CE. However, the abundant grain boundaries and surface defects of nanostructured Pt lead to poor conductivity.[35] Consequently, an ideal Pt-loaded support material should be endowed with a large specific surface area, excellent catalytic activity and high electrical conductivity to function as an efficient catalyst. A series of Pt-loaded nanocomposite CE materials have been developed by using different support materials, such as SiC,[36] multi-walled carbon nanotubes (MWCNTs),[34] carbon nanofibers,[37] graphene,[33] and polypyrrole nanospheres.[38] However, these reported support materials never demonstrated a comparable η to that of a conventional Pt CE.

[a]State Key Laboratory of Electronic Thin Film and Integrated Devices, University of Electronic Science and Technology of China, Chengdu 610054, P. R. China. E-mail: wangninguestc@gmail.com

[b]Integrated Composites Laboratory (ICL), Department of Chemical & Biomolecular Engineering, University of Tennessee, Knoxville, TN 37996, USA. E-mail: zguo10@utk.edu

† These authors contributed equally to this work.

This journal is © The Royal Society of Chemistry 2016

Published on 02 February 2016. Downloaded by University of Tennessee at Knoxville on 02/06/2016 19:25:03.

Herein, we report the synthesis of an ultra-lightweight carbon nanotube aerogel (CNA)[39,40] consisting of self-assembled, interconnected MWCNT skeletons, with a density of 110 mg cm^{-3}, a large specific surface area of 507.3 m^2 g^{-1}, a large porosity of >99%, high electrical conductivity, good electrochemical stability, high structural flexibility, and robustness. Our study shows that the well-organized mesoporous CNA exhibits better catalytic activity than MWCNTs and even Pt CEs. Furthermore, a small number of Pt nanoparticles loaded onto CNAs by thermal decomposition of H_2PtCl_6 to obtain a nanocomposite (CNA–Pt) CE led to a higher level of η. The use of CNAs as the support structure of Pt nanoparticles for the electrocatalytic reduction of I_3^- in DSSCs was disclosed for the first time.

2. Experimental

2.1 Synthesis of carbon nanotube aerogels (CNAs)

Typically, 0.05 g of MWCNTs (Nanocyl NC 7000, offered by Nanocyl, Belgium) were uniformly dispersed in distilled water (4.73 mL) by ultrasonic agitation. Subsequently, resorcinol (0.42 g), formaldehyde (0.64 g), and sodium carbonate (0.003 g) were dissolved in 1.52 mL distilled water to form a homogeneous solution, which was then poured into the MWCNT aqueous solution. The as-prepared mixture was aged in a glass beaker at 80 °C for 60 h to form hydrogels, followed by freeze-drying at liquid nitrogen temperature (−60 °C) for 24 h and then heat treatment at 1100 °C for 1 h in an Ar atmosphere to achieve ultra-light weight CNA products.

2.2 Preparation of CNA–Pt nanocomposites

The as-obtained CNAs were soaked in 40 mM H_2PtCl_6 dissolved in ethanol solution for 10 s and then dried at 120 °C for 30 min to remove residual ethanol. Afterwards, the dried CNA–Pt nanocomposites were heated at 400 °C for 30 min in an inert atmosphere for the reduction of H_2PtCl_6. This process allowed Pt nanoparticles to be adsorbed onto the surface of CNAs owing to the strong interaction induced by large specific surface energy. The above steps were repeated for obtaining different quantities of Pt nanoparticles supported on the CNAs. The content of Pt was roughly calculated by weighing the CNA before and after the deposition of Pt nanoparticles. Finally, a thin slice of CNA–Pt was transferred onto the transparent conducting oxide glass (FTO, sheet resistance 12 Ω $\square^{-1}$, purchased from Hartford Glass Co., USA). For a good comparison with bare CNA and CNA–Pt CEs, the conventional bare Pt and MWCNT CEs were also studied. The Pt CE was prepared by heating a thin layer of H_2PtCl_6 solution onto a FTO glass substrate at 400 °C for 30 min. The details of the preparation of the MWCNT CE can be found elsewhere.[17] Briefly, a binder solution was prepared by adding 0.16 g (carboxymethyl)-cellulose sodium salt into 19.84 mL distilled water, and then a total of 2.25 g MWCNTs was added followed by grinding to form a homogeneous MWCNT slurry. The resulting product was tape-cast onto a previously cleaned FTO glass substrate and then dried at 50 °C for 12 h in air.

2.3 Preparation of dye adsorbed photoanodes

The cleaned FTO conductive glass plates were coated with a compact layer of TiO_2 (~80 nm) by spin coating using a solution of 0.04 M tetra butyl titanate in isopropanol (containing 10 μL HCl per 5 mL solution), and then sintered at 500 °C for 30 min. Afterwards, the TiO_2 paste containing 18% commercial P25 TiO_2 nanoparticles, 9% ethyl cellulose and 73% terpineol was used for the deposition of a TiO_2 mesoporous layer (~8 μm) by the doctor-blade method, followed by heating under an air flow at 125 °C for 5 min, at 325 °C for 5 min, at 375 °C for 5 min, at 450 °C for 5 min, and at 500 °C for 15 min. After naturally cooling down to room temperature, the TiO_2 electrodes were immersed into a 0.12 M $TiCl_4$ solution at 70 °C for 30 min. After washing with water and drying in air, the samples were sintered at 500 °C for 30 min. After being cooled down to about 120 °C, the TiO_2 electrodes were immersed into a 0.5 mM ethanol solution of N719 dye ([*cis*-di(thiocyanato)-*N*,*N*′-bis(2,2′-bipyridyl-4-carboxylicacid)-4-tetrabutylammonium carboxylate]) (Solaronix Co., Ltd., Switzerland) and maintained at room temperature for 12 h. Afterwards, the as-prepared dye soaked photoanodes were washed in ethanol to remove physically adsorbed dye molecules before the cell assembly.

2.4 Assembly of DSSCs

The dye adsorbed TiO_2 photoanodes and various CEs were assembled to form DSSCs by sandwiching the electrolyte solution composed of 0.05 M I_2, 0.5 M LiI, and 0.5 M 4-*tert*-butylpyridine dissolved into 8 mL of acetonitrile. The active area of each cell was 3 mm × 3 mm.

2.5 Characterization

The surface morphologies and elemental composition of the CEs fabricated with the CNA and CNA–Pt were characterized by means of field emission scanning electron microscopy (FE-SEM, JSM-7500F, JEOL, Japan) and energy dispersive spectroscopy (EDS). High-resolution transmission electron microscopy (HR-TEM) images of CNA–Pt were obtained using a JEOL-2010HR TEM to further determine the intrinsic structure. The specific Brunauer–Emmett–Teller (BET) surface area was characterized on a Quadrasorb EVO QDS-30 by nitrogen adsorption at 77.4 K. Prior to each measurement, the synthesized CNAs with and without Pt nanoparticles were degassed at 300 °C for 12 h under high vacuum (<0.01 mbar). The pore size distribution of the nanocomposites was calculated by density functional theory (DFT).

The photocurrent density–voltage (*J*–*V*) tests of the DSSCs were performed under a solar simulator with AM 1.5G and 100 mW cm^{-2} illumination (Sun 3000 Solar Simulators, ABET Technologies, USA), which was calibrated by using a Si reference solar cell. The electrochemical impedance spectroscopy (EIS) measurements were carried out using full cells under standard irradiation using an electrochemical workstation (CHI660c, CHI Instrument, Co. Ltd., China). The frequency range of EIS experiments was set from 0.1 MHz to 100 mHz and the applied bias voltage was set at the open-circuit voltage of the

Published on 02 February 2016. Downloaded by University of Tennessee at Knoxville on 02/06/2016 19:25:03.

DSSC with an AC modulation signal of 10 mV. The Nyquist plots from EIS were analyzed using an equivalent circuit model by the Z-view software. Tafel polarization curves were determined by applying the same electrochemical workstation on the dummy cells with a scan rate of 10 mV s^{-1}.

3. Results and discussion

The microscopic surface morphologies of CNA and MWCNT CEs were examined by FE-SEM to demonstrate the structural differences. Fig. 1A and B show the FE-SEM images of CNAs at low and high magnifications, respectively. The CNTs are observed to be self-assembled into a porous, interconnected, and uniformly distributed three-dimensional framework structure. It should be noted that the diameter of CNTs in the CNA CE is observed to be a little larger than that in the MWCNT CE (see Fig. 1B and C). The graphitic treatment of CNAs at high temperatures allows for a lot of carbon particles to be left on the surface of CNTs due to the decomposition of organic solutes, leading to C–C bonding between the CNTs. Compared to the physical contact between CNTs for the MWCNT CE, the CNA CE exhibits more tight interconnection between them (see the rectangular boxes in Fig. 1B). Hence, the CNA CE has a remarkably low sheet resistance of 15.3 ± 0.3 Ω $\square^{-1}$ compared with the MWCNT CE (119.6 ± 1 Ω $\square^{-1}$). Fig. 1D gives the surface morphology of the CNA–Pt nanocomposite with 3.75 wt% Pt loading (CNA-3.75 wt% Pt). The Pt nanoparticles are homogeneously distributed in the matrix of CNAs, and the pore diameter of CNAs is significantly larger than the size of Pt nanoparticles. As evidenced from the inset of Fig. 1D, the energy dispersive spectroscopy (EDS) spectrum of the CNA–Pt nanocomposite clearly validates the presence of Pt and C, indicating that CNAs are successfully decorated with Pt nanoparticles. This is further testified by typical HR-TEM images of CNA-3.75 wt% Pt, Fig. 1D & E. Pt nanoparticles attached to CNAs exhibit obvious lattice fringes with a lattice spacing of 2.26 and 1.98 Å, which can be indexed to (111) and (200) planes of Pt, respectively.

The specific BET surface area and pore size distribution of the synthesized CNAs with and without loading Pt nanoparticles were characterized by using the nitrogen adsorption and desorption isotherms, Fig. 2. Fig. 2A(a)&(b) display the hysteresis loop, indicating the mesoporous properties of the CNA and CNA-3.75 wt% Pt. As shown in Table 1, it is found that the CNA has a BET specific surface area (SSA) of 507.3 m^2 g^{-1} with an average DFT pore diameter of 3.794 nm and a pore volume of 0.489 cm^3 g^{-1} while the CNA-3.75 wt% Pt has a 482.4 m^2 g^{-1} BET SSA with an average DFT pore diameter of 3.416 nm and a 0.402 cm^3 g^{-1} pore volume.

The CV measurements were carried out to evaluate the electrocatalytic activity of different CEs for the reduction of triiodide, as shown in Fig. 3. The relatively negative pair is attributed to the oxidation and reduction of I^-/I_3^-, which directly affect the photovoltaic performance of DSSCs.[36] Similar peak to peak splitting (E_{pp}) can be observed for Fig. 3a (E_{pp} = 400 mV) and Fig. 3d (E_{pp} = 412 mV), but it is little larger than that observed for the other two CEs. Moreover, Fig. 3d displays the lowest current density (J_{red} = −1.76 mA cm^{-2} and J_{ox} = 1.48 mA cm^{-2}), suggesting that the MWCNT has the poorest electrocatalytic activity towards the I^-/I_3^- redox reaction. In contrast, Fig. 3b shows similar E_{pp} (312 mV) but higher current densities (J_{red} = −2.35 mA cm^{-2} and J_{ox} = 2.09 mA cm^{-2}) compared to Fig. 3c (303 mV, J_{red} = −1.96 mA cm^{-2}, and J_{ox} = 1.74 mA cm^{-2}), indicating that the CNA-3.75 wt% Pt CE has the best electrocatalytic activity. From the CV results, we can conclude that loading a small number of Pt nanoparticles greatly improves its electrocatalytic activity due to the synergic effect of the CNA and Pt. It should be noted that the CNA with a high specific surface area and good conductivity significantly increases the electrochemically active surface area and thereby

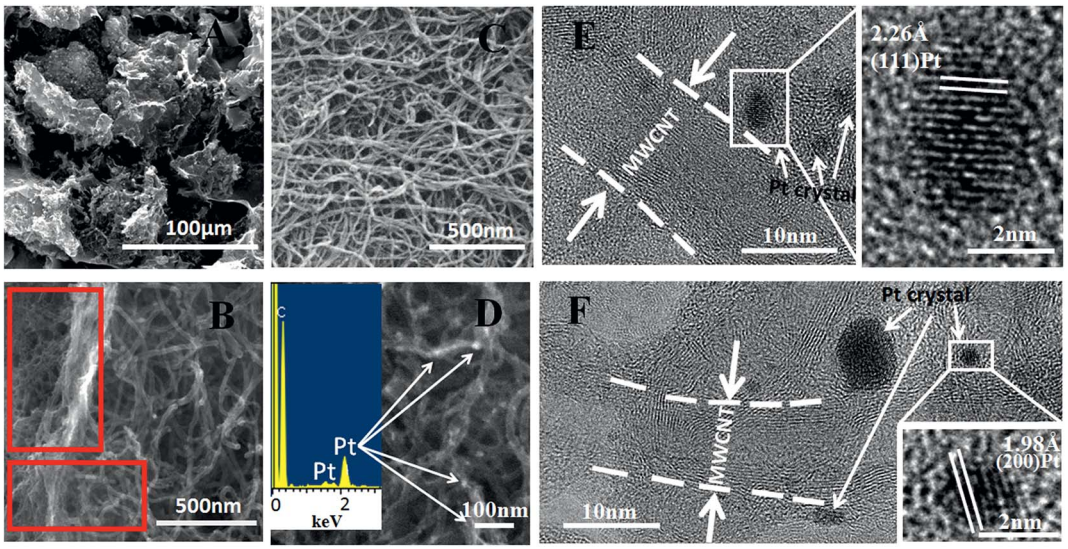

Fig. 1 FE-SEM images of the CNA ((A) low magnification; (B) high magnification), (C) MWCNTs, and (D) CNA-3.75 wt% Pt; the inset in (D) shows the EDS spectrum of CNA-3.75 wt% Pt. (E and F) representative HRTEM images observed from the CNA-3.75 wt% Pt nanofibers.

 This journal is © The Royal Society of Chemistry 2016

Published on 02 February 2016. Downloaded by University of Tennessee at Knoxville on 02/06/2016 19:25:03.

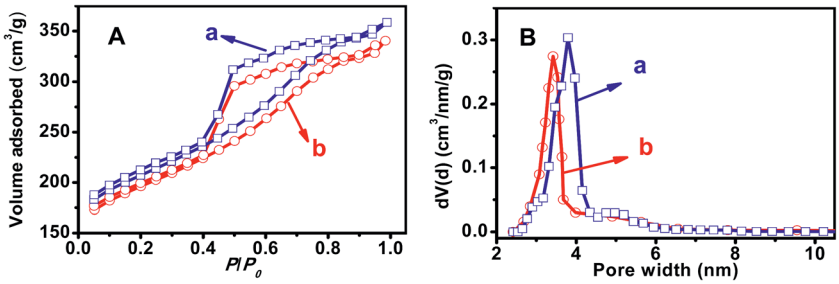

Fig. 2 N_2 adsorption–desorption isotherms (A) and pore size distributions (B) of the synthesized samples. (a) CNA and (b) CNA-3.75 wt% Pt.

Table 1 Structural properties of the CNA and CNA-3.75 wt% Pt

Samples	BET SSA ($m^2\ g^{-1}$)	Average pore size (nm)	Pore volume ($cm^3\ g^{-1}$)
CNA	507.3	3.794	0.489
CNA-3.75 wt% Pt	482.4	3.416	0.402

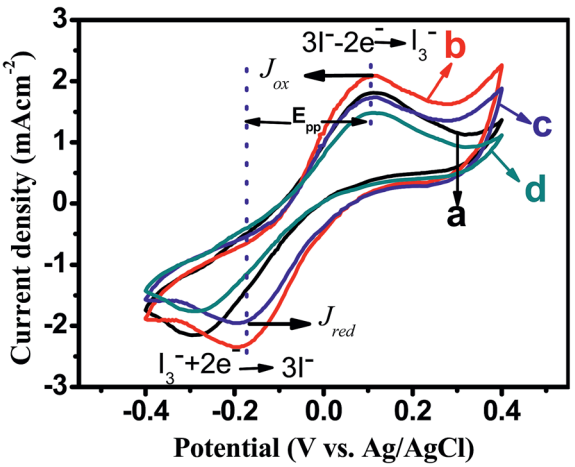

Fig. 3 CVs of CEs: (a) CNA CE, (b) CNA-3.75 wt% Pt CE, (c) conventional Pt CE, and (d) MWCNT CE in acetonitrile solution containing 10 mM LiI, 1 mM I_2 and 0.1 M $LiClO_4$ at a scan rate of 50 mV s^{-1}.

speeds up the reaction rate towards the reduction of I_3^- ions, exhibiting higher current density ($J_{red} = -2.15$ mA cm^{-2}, $J_{ox} = 1.81$ mA cm^{-2}) than the Pt CE.

Fig. 4A presents the current density–voltage (J–V) characteristics of the best performing DSSCs applying different CEs. As listed in Table 2, the DSSC with the MWCNT CE shows a short-circuit current density (J_{sc}) of 13.65 mA cm^{-2}, open-circuit voltage (V_{oc}) of 719 mV, fill factor $\left(FF = \frac{P_{max}}{V_{oc} \times J_{sc}}\right)$ of 0.61 and η of 5.95% ($\eta = P_{max}$%). In contrast, enhanced photovoltaic performance ($J_{sc} = 16.17$ mA cm^{-2}, FF = 0.68, $V_{oc} = 761$ mV, and $\eta = 8.35$%) can be observed for the CNA CE based DSSC, which should be attributed to a lower resistance of the CNA CE than that of the MWCNT CE. It is worth noting that the device with the conventional Pt CE displays a lower η (7.39%) than that applying the CNA CE, which is accordance with the corresponding results of CV analysis (see Fig. 3(a) and (c)). Moreover, the performance of the CNA CE based DSSC is superior to those of DSSCs that use most other support materials as CEs.[34,36,37,42,43]

In the meantime, the photovoltaic performances of the DSSCs applying the CNA–Pt CE with different amounts of Pt loading were further studied. Herein, the change range of photovoltaic parameters with the Pt loading can be gauged by dividing the standard deviations by the average value of respective parameters (denoted as σ). Fig. 4B exhibits the dependences of V_{oc} and FF on mass percentages of Pt and the calculated σ values of both the V_{oc} and FF are less than 1%. However, the σ value of J_{sc} reaches up to 3.3% (see Fig. 4C(a)), which significantly reflects that the content of Pt nanoparticles mainly affects the J_{sc} value but has little influence on the V_{oc} and FF fluctuations. The highest η of 9.04% can be achieved for the DSSC with the CNA-3.75 wt% Pt CE (see Fig. 4A(b) and 4C(b)), which is higher than those of the devices applying Pt/carbon support CEs.[33,34,37,42,44,45] There is a large improvement of 8.26 and 22.33% in η compared to that of the bare CNA and conventional Pt CE, respectively. Further increasing the Pt content causes serious aggregation of nanoparticles, leading to the decrease of the active surface area and dye regeneration ability. Hence, there could be an obvious reduction in J_{sc} and η when the Pt content was more than 3.75 wt%, Fig. 4C.

In order to provide insight into the charge transfer process and to further evaluate the electrochemical activity of CE materials, the EIS measurements were carried out under one sun illumination. Fig. 5A(a) and (b) demonstrate the Nyquist plots of the full cells with the CNA CE and CNA-3.75 wt% Pt CE, respectively. Two obvious arcs for each cell could be identified. The high frequency arc in the left region can be assigned to the charge-transfer resistance (R_{ct1}) and double layer capacitance (C_{dl1}) of the CE/electrolyte interface, while the intermediate frequency arc in the right region can be ascribed to the charge-transfer resistance (R_{ct2}) and double layer capacitance (C_{dl2}) at the dyed TiO_2/electrolyte interface. The R_s is the series resistance mainly composed of the sheet resistance of the CEs, FTO glass substrate, TiO_2 film, *etc.*[41] The inset of Fig. 5A displays a typical equivalent circuit diagram used to analyze the Nyquist plots by the Z-view software. The fitted parameters extracted from the Nyquist plots of the respective cells are summarized in Table 3. There are no significant differences in R_s for both cells, indicating that a small number of Pt nanoparticles loaded onto

Published on 02 February 2016. Downloaded by University of Tennessee at Knoxville on 02/06/2016 19:25:03.

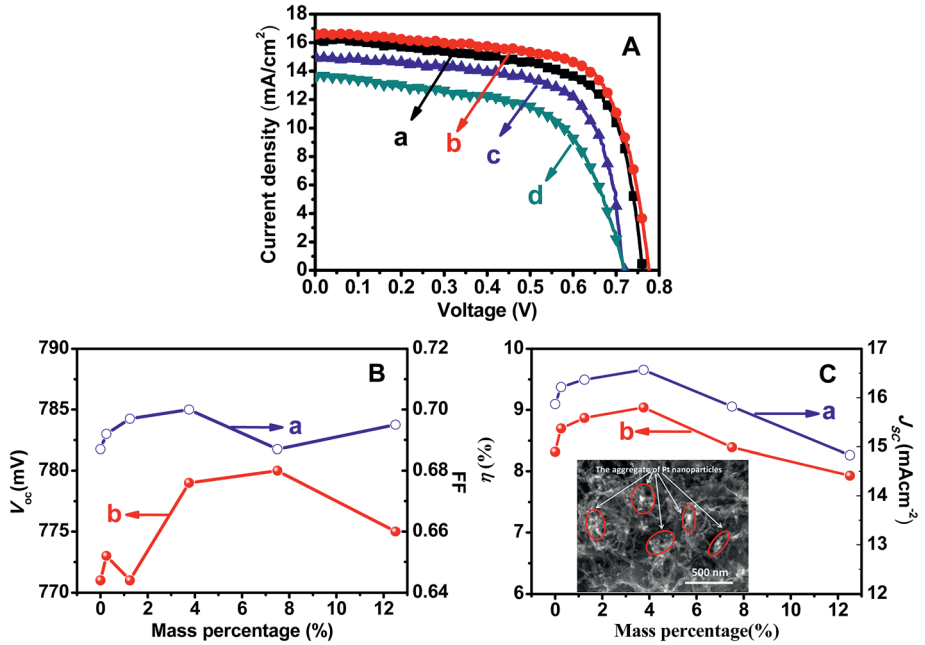

Fig. 4 (A) J–V characteristics of the best performing DSSCs using different CEs. (a) CNA CE, (b) CNA-3.75 wt% Pt CE, (c) conventional Pt CE, and (d) MWCNT CE; (B) FF (a) and V_{oc} (b) as a function of Pt loading on the CNAs; (C) J_{sc} (a) and η (b) as a function of Pt loading on the CNAs. The inset in (C) shows the aggregation of Pt nanoparticles.

Table 2 Photovoltaic parameters of DSSCs fabricated with different CEs under one sun illumination (AM 1.5G, 100 mW cm^{-2})[a]

CEs	J_{sc} (mA cm^{-2})	V_{oc} (mV)	FF	η_{max} (%)	$\eta_{average}$ (%)
Pt	14.89	723	0.69	7.39	7.01 ± 0.38
MWCNTs	13.65	719	0.61	5.95	5.73 ± 0.22
CNA	16.17	761	0.68	8.35	8.06 ± 0.29
CNA-3.75 wt% Pt	16.57	779	0.70	9.04	8.77 ± 0.27

[a] Average η ($\eta_{average}$) with error ranges and the highest (η_{max}) that are recorded efficiencies when all the devices were fabricated under the same conditions for valid comparisons.

Table 3 The simulated EIS parameters of the full cells based on the CNA CE and CNA-3.75 wt% Pt CE

CE	R_s (Ω cm^2)	R_{ct1} (Ω cm^2)	C_{dl1} (F)	R_{ct2} (Ω cm^2)	C_{dl2} (F)
CNA	1.99	1.16	2.28×10^{-5}	6.70	2.04×10^{-4}
CNA-3.75 wt% Pt	1.95	0.83	1.77×10^{-5}	6.12	1.46×10^{-4}

CNAs would not change significantly the CE conductivity. Fig. 5A(b) shows a lower R_{ct1} (0.83 Ω cm^2) than Fig. 5A(a) (1.16 Ω cm^2), suggesting relatively faster electron exchange and higher reduction rates of redox couples at the interface of the CNA-3.75 wt% Pt CE and electrolyte, in good agreement with the C–V and J–V results. It is also noted that the R_{ct2} varies obviously less than the R_{ct1} due to the same photoanode structure.

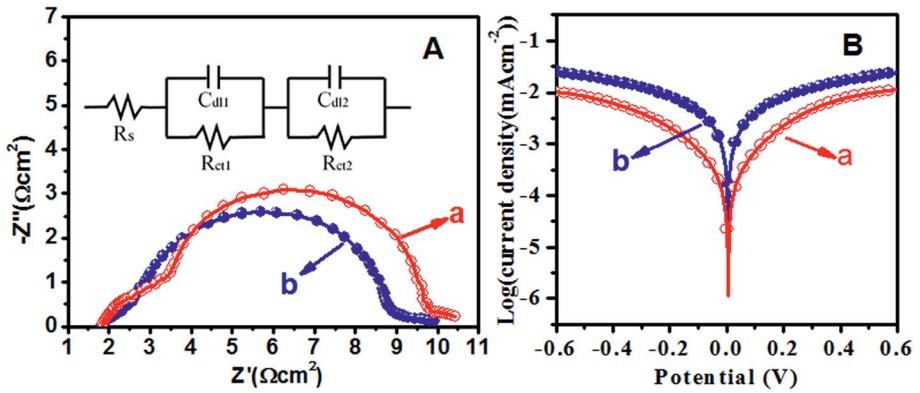

Fig. 5 (A) Nyquist plots of the full cells and (B) Tafel curves of the symmetrical cells fabricated with the (a) bare CNA CE and (b) CNA-3.75 wt% Pt CE. The inset in (A) shows an equivalent circuit for fitting Nyquist plots.

 This journal is © The Royal Society of Chemistry 2016

Published on 02 February 2016. Downloaded by University of Tennessee at Knoxville on 02/06/2016 19:25:03.

To further characterize the catalytic activities of the I_3^-/I^- couple on the CE surface, Fig. 5B(a) and (b) present the Tafel polarization curves of dummy cells fabricated with the CNA CE and CNA-3.75 wt% Pt CE, respectively. The exchange current density (J_0) and the limiting diffusion current density (J_{lim}) can be obtained according to Tafel curves, which are closely related to the catalytic activity of CEs. Apparently, Fig. 5B(b) exhibits higher J_{lim} than Fig. 5B(a), suggesting that the CNA-3.75 wt% Pt CE has a higher diffusion rate for the redox couple in the electrolyte than the CNA CE. Additionally, the slope of the curve in Fig. 5B(b) is larger than that of the one in Fig. 5B(a), indicating an enhanced J_0 and catalytic activity for the Pt-loaded nanocomposites, in accordance with the EIS and CV results.

Overall, the CNA CE with a large specific surface area and good electrical conductivity exhibits better catalytic activity of I_3^-/I^- and photovoltaic performance than the conventional Pt CE and MWCNT CE. The performance of the CNA based device is further enhanced by introducing Pt nanoparticles, which is mainly attributed to the improved electrocatalytic activity, reduced R_{ct} at the CE/electrolyte interface and increased diffusion rate for the redox couple in the electrolyte.

4. Conclusions

As a highly efficient CE material for the DSSC device, the carbon nanotube aerogels with interconnected three dimensional network nanostructures demonstrated superior electrocatalytic activity and photovoltaic performance compared to the conventional MWCNT CE and Pt CE, which mainly result from the large SSA and high electrical conductivity. Furthermore, the device with the CNA-3.75 wt% Pt CE reveals further improvement in the electrocatalytic activity and PCE (9.04%), corresponding to an increase of 8.26 and 22.33% compared to the bare CNA CE and Pt CE based device, respectively. Such an enhancement highlights the predominant synergic effect of CNAs and Pt nanoparticles, in which the R_{ct1} at the CE/electrolyte interface and diffusion rate for the redox couple in the electrolyte can be significantly improved. When the loaded Pt nanoparticles were uniformly dispersed on CNAs, a higher η could be achieved. Hence, this work highlights the potential of employing CNAs as a support for loading a small number of noble metal Pt to obtain superior electrocatalytic activity and photovoltaic performance, which fully meet the large-scale industrial applications of cost-effective DSSCs.

Acknowledgements

This work was financial supported by China-Japan International Cooperation Program Funds (No. 2010DFA61410 and 2011DFA50530), National Natural Science Foundations of China (No. 51272037, 51272126, 51303116 and 51472043) and Program for New Century Excellent Talents in University (No. NCET-12-0097). Z. Guo appreciates the start-up funds from the University of Tennessee.

Notes and references

1 B. O'Regan and M. Grätzel, *Nature*, 1991, **353**, 737–740.
2 A. Kay and M. Grätzel, *Sol. Energy Mater. Sol. Cells*, 1996, **44**, 99–117.
3 M. Grätzel, *Nature*, 2001, **414**, 338–344.
4 Q. Wang, S. Ito, M. Grätzel, F. Fabregat-Santiago, I. n. Mora-Seró, J. Bisquert, T. Bessho and H. Imai, *J. Phys. Chem. B*, 2006, **110**, 25210–25221.
5 M. Grätzel, *Acc. Chem. Res.*, 2009, **42**, 1788–1798.
6 D. Kuang, C. Klein, S. Ito, J. E. Moser, R. Humphry-Baker, N. Evans, F. Duriaux, C. Grätzel, S. M. Zakeeruddin and M. Grätzel, *Adv. Mater.*, 2007, **19**, 1133–1137.
7 S. Ito, T. N. Murakami, P. Comte, P. Liska, C. Grätzel, M. K. Nazeeruddin and M. Grätzel, *Thin Solid Films*, 2008, **516**, 4613–4619.
8 H. Su, M. Zhang, Y. H. Chang, P. Zhai, N. Y. Hau, Y. T. Huang, C. Liu, A. K. Soh and S. P. Feng, *ACS Appl. Mater. Interfaces*, 2014, **6**, 5577–5584.
9 T. N. Murakami and M. Grätzel, *Inorg. Chim. Acta*, 2008, **361**, 572–580.
10 M. Wang, A. M. Anghel, B. Marsan, N.-L. C. Ha, N. Pootrakulchote, S. M. Zakeeruddin and M. Grätzel, *J. Am. Chem. Soc.*, 2009, **131**, 15976–15977.
11 S. Yun, L. Wang, W. Guo and T. Ma, *Electrochem. Commun.*, 2012, **24**, 69–73.
12 D. W. Zhang, X. D. Li, H. B. Li, S. Chen, Z. Sun, X. J. Yin and S. M. Huang, *Carbon*, 2011, **49**, 5382–5388.
13 A. Hagfeldt, G. Boschloo, L. Sun, L. Kloo and H. Pettersson, *Chem. Rev.*, 2010, **110**, 6595–6663.
14 D. Liu, M. Zhao, Y. Li, Z. Bian, L. Zhang, Y. Shang, X. Xia, S. Zhang, D. Yun, Z. Liu, A. Cao and C. Huang, *ACS Nano*, 2012, **6**, 11027–11034.
15 E. Ramasamy, W. J. Lee, D. Y. Lee and J. S. Song, *Appl. Phys. Lett.*, 2007, **90**, 173103.
16 W. J. Lee, E. Ramasamy, D. Y. Lee and J. S. Song, *Sol. Energy Mater. Sol. Cells*, 2008, **92**, 814–818.
17 W. J. Lee, E. Ramasamy, D. Y. Lee and J. S. Song, *ACS Appl. Mater. Interfaces*, 2009, **1**, 1145–1149.
18 P. Joshi, L. Zhang, Q. Chen, D. Galipeau, H. Fong and Q. Qiao, *ACS Appl. Mater. Interfaces*, 2010, **2**, 3572–3577.
19 W. Ke, G. Fang, H. Tao, P. Qin, J. Wang, H. Lei, Q. Liu and X. Zhao, *ACS Appl. Mater. Interfaces*, 2014, **6**, 5525–5530.
20 Z. Tachan, M. Shalom, I. Hod, S. Rühle, S. Tirosh and A. Zaban, *J. Phys. Chem. C*, 2011, **115**, 6162–6166.
21 Z. Yang, C.-Y. Chen, C.-W. Liu, C.-L. Li and H.-T. Chang, *Adv. Energy Mater.*, 2011, **1**, 259–264.
22 J. T. Park, C. S. Lee and J. H. Kim, *Nanoscale*, 2015, **7**, 670–678.
23 S. Shukla, N. H. Loc, P. P. Boix, T. M. Koh, R. R. Prabhakar, H. K. Mulmudi, J. Zhang, S. Chen, C. F. Ng, C. H. A. Huan, N. Mathews, T. Sritharan and Q. Xiong, *ACS Nano*, 2014, **8**, 10597–10605.
24 Q. W. Jiang, G. R. Li and X. P. Gao, *Chem. Commun.*, 2009, **44**, 6720–6722.
25 C. Tan, J. Cao, A. M. Khattak, F. Cai, B. Jiang, G. Yang and S. Hu, *J. Power Sources*, 2014, **270**, 28–33.

Published on 02 February 2016. Downloaded by University of Tennessee at Knoxville on 02/06/2016 19:25:03.

26 Z. S. Wu, A. Winter, L. Chen, Y. Sun, A. Turchanin, X. Feng and K. Mullen, *Adv. Mater.*, 2012, **24**, 5130–5135.
27 M. Wu, X. Lin, A. Hagfeldt and T. Ma, *Angew. Chem., Int. Ed.*, 2011, **50**, 3520–3524.
28 M. Wu, X. Lin, A. Hagfeldt and T. Ma, *Chem. Commun.*, 2011, **47**, 4535–4537.
29 J. Xia, C. Yuan and S. Yanagida, *ACS Appl. Mater. Interfaces*, 2010, **2**, 2136–2139.
30 J. Wan, G. Fang, H. Yin, X. Liu, D. Liu, M. Zhao, W. Ke, H. Tao and Z. Tang, *Adv. Mater.*, 2014, **26**, 8101–8106.
31 B. He, X. Meng and Q. Tang, *ACS Appl. Mater. Interfaces*, 2014, **6**, 4812–4818.
32 Q. Li, J. Wu, Q. Tang, Z. Lan, P. Li, J. Lin and L. Fan, *Electrochem. Commun.*, 2008, **10**, 1299–1302.
33 V. D. Dao, L. V. Nang, E. T. Kim, J. K. Lee and H. S. Choi, *ChemSusChem*, 2013, **6**, 1316–1319.
34 J. W. Guo, B. Zhang, Y. Hou, S. Yang, X. H. Yang and H. G. Yang, *J. Mater. Chem. A*, 2013, **1**, 1982–1986.
35 G. R. Li, F. Wang, Q. W. Jiang, X. P. Gao and P. W. Shen, *Angew. Chem., Int. Ed.*, 2010, **49**, 3653–3656.
36 S. Yun, L. Wang, C. Zhao, Y. Wang and T. Ma, *Phys. Chem. Chem. Phys.*, 2013, **15**, 4286–4290.
37 S. I. Noh, T.-Y. Seongb and H.-J. Ahn, *J. Ceram. Process Res.*, 2012, **13**, 491–494.
38 S. S. Jeon, C. Kim, J. Ko and S. S. Im, *J. Phys. Chem. C*, 2011, **115**, 22035–22039.
39 (*a*) H. Sun, Z. Xu and C. Gao, *Adv. Mater.*, 2013, **25**, 2554–2560; (*b*) H. Wang, Z. Xu, H. Yi, H. Wei, Z. Guo and X. Wang, *Nano Energy*, 2014, **7**, 86–96.
40 M. A. Worsley, P. J. Pauzauskie, T. Y. Olson, J. Biener, H. Joe, J. Satcher and T. F. Baumann, *J. Am. Chem. Soc.*, 2010, **132**, 14067–14069.
41 Q. Wang, J.-E. Moser and M. Grätzel, *J. Phys. Chem. B*, 2005, **109**, 14945–14953.
42 H. Y. Wang, F. M. Wang, Y. Y. Wang, C. C. Wan, B. J. Hwang, R. Santhanam and J. Rick, *J. Phys. Chem. C*, 2011, **115**, 8439–8446.
43 Y. Zhao, A. Thapa, Q. Feng, M. Xi, Q. Qiao and H. Fong, *Nanoscale*, 2013, **5**, 11742–11747.
44 G. Yue, J. Wu, Y. Xiao, M. Huang, J. Lin, L. Fan and Z. Lan, *Electrochim. Acta*, 2013, **92**, 64–70.
45 P. T. Shih, R. X. Dong, S. Y. Shen, R. Vittal, J. J. Lin and K. C. Ho, *J. Mater. Chem. A*, 2014, **2**, 8742–8748.

 This journal is © The Royal Society of Chemistry 2016